Reactive Transport Modeling to Study Changes in Water Chemistry Induced by CO_2 Injection at the Frio-I Brine Pilot

Tianfu Xu[1], Yousif K. Kharaka[2], Christine Doughty [1], Barry M. Freifeld[1], and Thomas M. Daley[1]

[1]Earth Sciences Division, Lawrence Berkeley National Laboratory, 1 Cyclotron Road, Berkeley, CA 94720

[2]U.S. Geological Survey, MS/427, 345 Middlefield Rd., Menlo Park, CA 94025

Abstract. To demonstrate the potential for geologic storage of CO_2 in saline aquifers, the Frio-I Brine Pilot was conducted, during which 1600 tons of CO_2 were injected into a high-permeability sandstone and the resulting subsurface plume of CO_2 was monitored using a variety of hydrogeological, geophysical, and geochemical techniques. Fluid samples were obtained before CO_2 injection for baseline geochemical characterization, during the CO_2 injection to track its breakthrough at a nearby observation well, and after injection to investigate changes in fluid composition and potential leakage into an overlying zone. Following CO_2 breakthrough at the observation well, brine samples showed sharp drops in pH, pronounced increases in HCO_3^- and aqueous Fe, and significant shifts in the isotopic compositions of H_2O and dissolved inorganic carbon. Based on a calibrated 1-D radial flow model, reactive transport modeling was performed for the Frio-I Brine Pilot. A simple kinetic model of Fe release from the solid to aqueous phase was developed, which can reproduce the observed increases in aqueous Fe concentration. Brine samples collected after half a year had lower Fe concentrations due to carbonate precipitation, and this trend can be also captured by our modeling. The paper provides a method for estimating potential mobile Fe inventory, and its bounding concentration in the storage formation from limited observation data. Long-term simulations show that the CO_2 plume gradually spreads outward due to capillary forces, and the gas saturation gradually decreases due to its dissolution and precipitation of carbonates. The gas phase is predicted to disappear after 500 years. Elevated aqueous CO_2 concentrations remain for a longer time, but eventually decrease due to carbonate precipitation. For the Frio-I Brine Pilot, all injected CO_2 could ultimately be sequestered as carbonate minerals.

Keywords: CO_2 sequestration, Frio Formation, Water chemistry, Iron release, Reactive transport modeling

1

1. Introduction

Concern over the consequences of global warming due to increasing levels of anthropogenic carbon dioxide (CO_2) in the atmosphere has led to a variety of proposals to curtail, if not prevent, further increases. One such approach is to inject CO_2, captured from stationary sources (such as fossil-fuel power plants) into reasonably accessible structural reservoirs in deep permeable geologic formations. Candidate formations include deep saline aquifers in sedimentary basins, structural traps in depleted oil and gas fields, and deep unmineable coal seams (Bachu et al., 1994; Hitchon et al., 1999). Injecting CO_2 into saline formations in sedimentary basins is one of the most promising methods of geological storage of CO_2 for the long-term sequestration of the gas. This is because saline formations are ubiquitous to sedimentary basins (Hitchon et al., 1999; Gunter et al., 2000), they have enough capacity to store large amounts of CO_2 from anthropogenic emissions, and there are shorter distances between most large CO_2 point sources and saline formations, which can minimize CO_2 transportation costs (Soong et al., 2004; Allen et al., 2005; Zerai et al., 2006).

The Frio-I Brine Pilot was conducted to demonstrate the potential for geologic storage of CO_2 in saline aquifers (Hovorka et al., 2006). Approximately 1600 tons of CO_2 were injected during October 2004 through a single injection well into a sandstone, the ''C'' zone, of the Oligocene Frio Formation – a regional petroleum and brine reservoir in the U.S. Gulf Coast. An old oil-producing well penetrating the "C" zone located about 30 m up-dip from the injection well was recompleted and perforated as an observation well. Downhole and wellhead samples of formation water and gas from the ''C'' zone of both the injection and observation wells, and the overlying ''B'' zone (sandstone formation) of the observation well, were obtained using a variety of sampling tools and methodologies (Kharaka et al., 2009). Samples were obtained before CO_2 injection for baseline geochemical characterization, during the CO_2 injection to track its breakthrough at the observation well, and after injection to investigate changes in fluid composition and potential leakage into the overlying "B" zone (Freifeld et al., 2005; Kharaka et al. 2006a).

Following CO_2 breakthrough, samples showed sharp drops in pH (6.5-5.7) measured at surface after degassing, pronounced increases in HCO_3^- (100-3000 mg/L)

and dissolved Fe (30-1100 mg/L), and significant shifts in the isotopic compositions of H_2O and dissolved inorganic carbon (Kharaka et al., 2006b). There were also increases in the concentration of other metals, including Zn and Pb, which are generally sorbed and coprecipitated with iron oxyhydroxides (Kharaka et al., 2009). Injected CO_2 could also mobilize toxic organic compounds such as toluene and benzene. Environmental impacts could be major if large brine volumes with mobilized toxic metals and organics migrated into potable groundwater (Kharaka et al., 2009).

Preliminary modeling of CO_2/brine multi-phase flow for the Frio-I Brine Pilot has been performed previously (Hovorka et al., 2006; Doughty et al., 2008). For the present study, we perform reactive transport modeling based on detailed fluid and mineral compositions, and using a calibrated multi-phase flow model. The objectives of the present modeling are to understand changes in inorganic chemistry, Fe in particular, induced by CO_2 injection at the Frio-I Brine Pilot test site, to capture variations of aqueous concentrations over time at the observation well, and to investigate the long-term storage of CO_2 in gas, liquid and solid phases.

2. Regional Setting and Experimental Methods

The Frio site is located on the flank of a salt dome within the South Liberty oil field, near Dayton, Texas, a region of the Gulf Coast where industrial sources of CO_2 are abundant (Figure 1). Most of the wells in this field were drilled in the 1950s, with oil production from the Eocene Yegua Formation at depths of 2900 m. An inactive oil well, the Sun-Gulf-Humble Fee Tract 1, well #4 (SGH04, Figure 1), was recompleted and perforated in the Frio "C" sandstone at 1528-1534 m depth for use as an observation borehole. About 30 m downdip, a new CO_2 injection well was drilled and perforated, also in Frio "C" at 1541-1546 m (SGH03, Figure 1). The fluid at the "C" zone has a pressure of about 152 bar and a temperature of about 59^oC. The Frio Formation is composed of several reworked fluvial sandstone and siltstone beds that are separated by transgressive marine shales. Situated immediately above the "C" sandstone, the "B" sandstone has a 4-m-thick reworked fluvial sandstone bed at the top, but has more shale and siltstone beds, including a 7-m-thick transgressive marine shale bed at the bottom. However, the main

barrier to CO_2 leakage to the surface is expected to be the overlying regional thick marine shale beds of the Miocene-Oligocene Anahuac Formation (Hovorka et al., 2006).
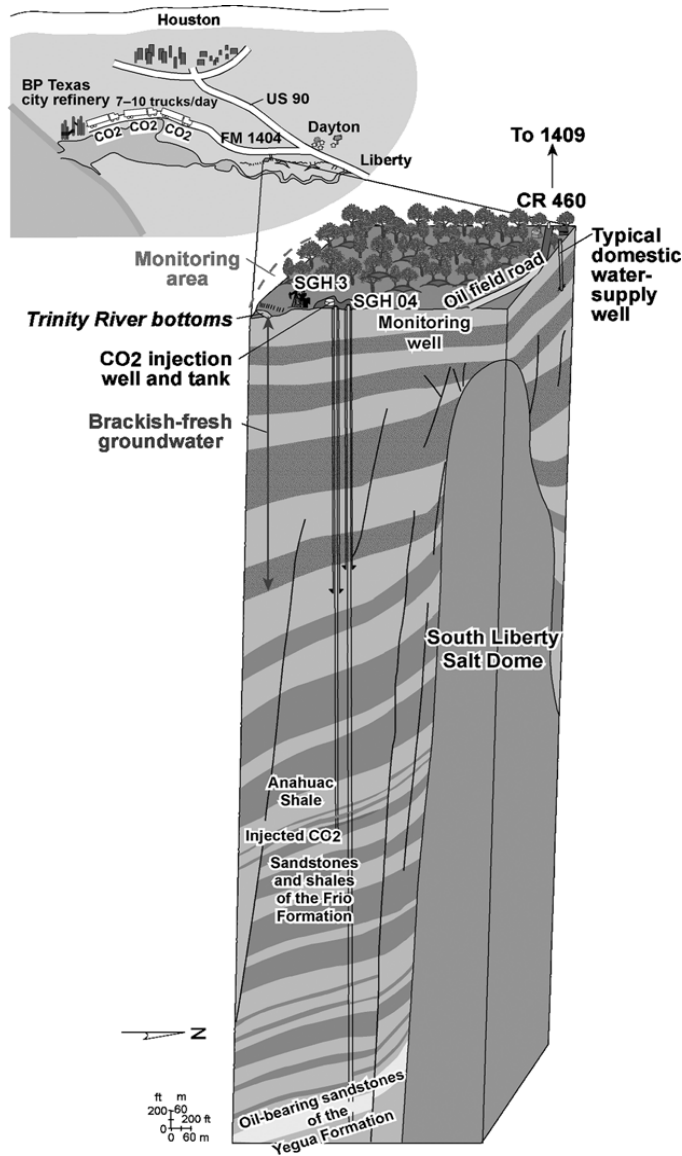

Figure 1. Location of the Frio Brine Pilot field site, 60 km from Houston, Texas, and a schematic of the underlying stratigraphy. CO_2 was injected in the Frio Formation, capped by the low-permeability Anahuac Shale. (Courtesy S. Hovorka)

Approximately 1600 tons of CO_2 were injected at a rate of about 3 kg/s during 4-14 October 2004. The pressure response was measured downhole at both the injection well and the observation well (Hovorka et al., 2006). Figure 2 shows variations in downhole pressure at the injection well together with variations in injection rate. The CO_2 injection rate was held as constant as possible except for two short-duration pump failure and two planed injection shutdowns designed to measure any pressure fall-off.
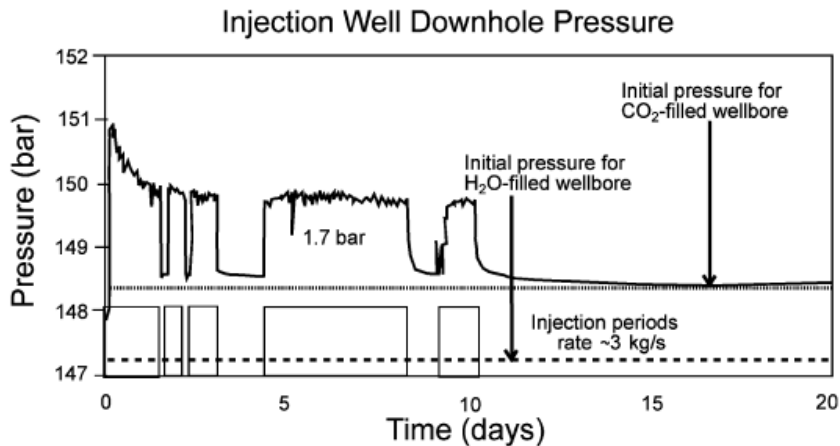

Figure 2. Variations in downhole pressure at the injection well together with variations in injection rate. (Courtesy S. Hovorka)

Pre- and post-injection fluid samples were obtained from both wells at the wellhead using gas lift by either N_2 or the injected CO_2, and downhole using evacuated Kuster samplers or the Schlumberger Modular Formation Dynamics Tester syringe-like tool (Freifeld et al., 2005; Kharaka et al., 2006a). During the CO_2 injection, intensive fluid sampling was conducted, with gas samples obtained from the top of the observation well and from the CO_2 injection line, and multiphase fluid samples collected from the observation well using the novel U-tube system developed for this field experiment (Freifeld et al., 2005). Water samples were collected from the start of injection until about noon, 7 October, when water became a minor component of fluid, but gas sampling continued until the end of injection. Acquiring frequent samples was necessary to track the arrival of CO_2, to investigate changes in the fluid compositions caused by CO_2 injection, and for geochemical modeling to investigate gas-water-rock interactions. Water

and gas samples collected were subjected to on-site and laboratory chemical and isotopic analyses by methodologies described in details in Kharaka and Hanor (2007) and Kharaka et al., (2009). These analyses permitted to track the arrival of CO_2 at the observation well, to provide an estimate of the irreducible brine saturation, and to quantify tracer breakthrough curves (Freifeld et al., 2005).

3. Simulation Tool

The present simulations employed the nonisothermal reactive transport code TOUGHREACT (Xu and Pruess, 2001; Xu et al., 2006). This code introduces reactive chemistry into the multiphase fluid and heat flow code TOUGH2 (Pruess, 2004). A new fluid property module, ECO2N, based on Spycher and Pruess (2005) work was used. This module provides an accurate description of the thermophysical properties of mixtures of water and CO_2 under conditions typically encountered in saline aquifers of interest for CO_2 sequestration ($31°C \leq T \leq 110°C$; 73.8 bars $< P \leq 600$ bars).

The numerical method for fluid flow and chemical transport simulations is based on the integral finite difference (IFD) method for space discretization. The IFD method provides flexible discretization of geologic media by allowing the use of irregular grids, which is well suited for simulation of flow, transport, and fluid-rock interaction in heterogeneous and fractured rock systems with varying petrology. For regular grids, the IFD method is equivalent to the conventional finite different method. An implicit time-weighting scheme is used for the flow, transport and kinetic geochemical equations. A sequential iterative approach is used for the coupling between transport and geochemical reactions. The model can be applied to one-, two-, or three-dimensional porous and fractured media with physical and chemical heterogeneity.

The model can accommodate any number of chemical species present in the liquid, gas and solid phases. A broad range of subsurface thermal-physical-chemical processes are considered under various thermohydrological and geochemical conditions of pressure, temperature, water saturation, ionic strength, and pH and Eh. Further details on the process capabilities are given in Xu and Pruess (2001) and Xu et al. (2006). In addition to all processes in TOUGHREACT (Xu et al., 2006), a kinetic model for release

of Fe from the solid to aqueous phase was developed in this work as described in details below (Section 4.5).

Note that modeling chemical changes in the CO_2 sequestration system studied here, requires a tool that can deal with a CO_2-water multi-phase flow and calculate dynamically partial pressures at each grid block and each time step. A conventional geochemical modeling tool such as PHREEQC (Parkhurst and Appelo, 1999) cannot be used because it can only cope with a single-phase water flow under one-dimensional constant flow velocity conditions. By using the comprehensive simulation tool like TOUGHREACT, more complex multi-dimensional problems can be addressed that especially involve multiphase fluid and heat flow, and geochemical interaction.

4. Model Setup

4.1. Flow conditions

Several three-dimensional multi-phase flow models have been developed for the Frio-I Brine Pilot test site (Doughty and Pruess, 2004; Doughty et al., 2008), each employing tens of thousands of grid blocks. However, when reactive transport is modeled, such a large number of grid blocks are impractical. Thus, for the present study of reactive transport modeling, a calibrated (in terms of density data of mixture of brine and CO_2) 1-D radial flow model with only 226 grid blocks was used.

A U-tube was used to collect a 52-L sample from the observation well every 2 hours, which was weighed at the surface while being maintained at downhole pressure conditions of about 150 bars (Freifeld et al., 2005). A decrease in sample density from that of formation brine (~1,068 kg/m^3) indicates CO_2 arrival to the observation well. The 1-D flow model was designed to match the CO_2 arrival time at the observation well, by setting the irreducible water saturation S_{lr} to an artificially high number ($S_{lr} = 0.75$). The irreducible water saturation S_{lr} is originally defined as a fraction of the pore volume occupied by water in a storage reservoir at maximum supercritical CO_2 phase saturation. It represents the layer of adsorbed water coating solid surfaces and the pendular water around grain contacts and at pore throats. However, here the calibrated high number S_{lr}, accounts for the fact that (1) non-uniform sweep may occur as a result of formation

heterogeneities or/and (2) buoyancy forces would tend to drive CO_2 towards the top of the storage formation. Assigning a large S_{lr} allows the CO_2 to bypass brine and thereby match the arrival time observed in the field.

To capture the concentration evolution of aqueous species at the observation well, the 1-D radial flow model used could be a reasonable approach. Another justification for using a 1-D radial model is that samples collected at the observation well are a mixture of waters from all along the vertical column of the U-tube. The 1-D model can be viewed as a depth-average 2-D model in terms of CO_2 gas saturation. Hydrogeological parameters for the 1-D radial flow problem (model), which solves governing equations for a two-phase (liquid-gas) and three-component (CO_2, water, and dissolved solid) system, are listed in Table 1.

Table 1. Hydrogeological parameters for the 1-D radial CO_2 injection problem according to (Doughty et al., 2008).

Aquifer thickness	5.5 m
Permeability (horizontal)	2.3×10^{-12} m^2
Porosity	0.34
Compressibility	2.1×10^{-9} Pa^{-1}
Temperature	59^0C
Pressure	152 bar
CO_2 injection rate	3 kg/s
Relative permeability	
Liquid (van Genuchten, 1980): $$k_{rl} = \sqrt{S^*}\left\{1 - \left(1 - \left[S^*\right]^{1/m}\right)^m\right\}^2$$ irreducible water saturation exponent	$S^* = (S_1 - S_{lr})/(1 - S_{lr})$ $S_{lr} = 0.75$ $m = 0.917$
Gas (Corey, 1954): $$k_{rg} = (1 - \widehat{S})^2 (1 - \widehat{S}^2)$$ residual gas saturation	$\widehat{S} = \dfrac{(S_1 - S_{lr})}{(1 - S_{lr} - S_{gr})}$ $S_{gr} = 0.01$
Capillary pressure	

Van Genuchten (1980) $$P_{cap} = -P_0\left(\left[S^*\right]^{-1/m} - 1\right)^{1-m}$$ irreducible water saturation
    exponent
    strength coefficient
	$S^* = (S_1 - S_{lr})/(1 - S_{lr})$
	 $S_{lr} = 0.03$
	 $m = 0.4118$
	 $P_0 = 3.953\,kPa$

4.2. Geochemical system

The Frio "C" zone is a subarkosic fine-grained, moderately sorted quartz and feldspar sandstone, with minor amounts of illite or smectite and calcite. The initial rock mineral composition used in the modeling is presented in Table 2, which may be broadly representative of US Gulf Coast sandstone formations (Xu et al., 2004, 2005 and 2007). The plagioclase at this site, as is the case with the Frio sandstones has an oligoclase composition. In the simulation, oligoclase was assumed to have a 1:4 of anorthite ($CaAl_2Si_2O_8$) over albite ($NaAlSi_3O_8$). The resulting composition is $CaNa_4Al_6Si_{14}O_{40}$, which closely represents the composition of oligoclase actually found in many arkosic sandstones (Newton et al., 1980). The selection of chlorite, illite and smectite composition is discussed in Xu et al. (2004, 2005)

Magnesite, dolomite, siderite, ankerite, dawsonite, and Ca-smectite could be formed after CO_2 injection and are specified as secondary minerals in the simulations. Almost all possibilities of secondary carbonate and clay minerals are covered in our simulations, which are based on previous studies of modeling (Xu et al., 2005, 2006, 2007; Gaus et al., 2005; White et al., 2005), laboratory experiments (Wolf et al., 2004; Chen et al., 2006; Bénézeth et al., 2007, 2009), and field observations (Watson et al., 2004; Moore et al., 2005; Worden 2006).

Table 2. Parameters for calculating kinetic rate constants of minerals. Note that: (1) all rate constants are listed for dissolution; (2) A is specific surface area, k_{25} is kinetic constant at 25°C, E_a is activation energy, and n is the power term (Eq. A.2); (3) the power term n for both acid and base mechanisms are with respect to H^+; (4) for pyrite, the neutral mechanism has n with respect to $O_2(aq)$, the acid mechanism has two species involved: one n with respect to H^+ and another n with respect to Fe^{3+}.

Mineral	Vol.% Of solid	A (cm²/g)	Neutral mechanism		Acid mechanism			Base mechanism		
			k_{25} (mol/m²/s)	E_a (KJ /mol)	k_{25}	E_a	$n(H^+)$	k_{25}	E_a	$n(H^+)$
Primary:										
Quartz	57.888	9.8	1.023×10^{-14}	87.7						
Kaolinite	2.015	151.6	6.918×10^{-14}	22.2	4.898×10^{-12}	65.9	0.777	8.913×10^{-18}	17.9	-0.472
Calcite	1.929	9.8	1.549×10^{-6}	23.5	5.012×10^{-1}	14.4	1.0			
Illite	0.954	151.6	1.660×10^{-13}	35	1.047×10^{-11}	23.6	0.34	3.020×10^{-17}	58.9	-0.4
Oligoclase	19.795	9.8	1.445×10^{-12}	69.8	2.138×10^{-10}	65	0.457			
K-feldspar	8.179	9.8	3.890×10^{-13}	38	8.710×10^{-11}	51.7	0.5	6.310×10^{-22}	94.1	-0.823
Na-smectite	3.897	151.6	1.660×10^{-13}	35	1.047×10^{-11}	23.6	0.34	3.020×10^{-17}	58.9	-0.4
Chlorite	4.556	151.6	3.02×10^{-13}	88	7.762×10^{-12}	88	0.5			
Hematite	0.497	12.9	2.512×10^{-15}	66.2	4.074×10^{-10}	66.2	1			
Secondary:										
Magnesite		9.8	4.571×10^{-10}	23.5	4.169×10^{-7}	14.4	1			
Dolomite		9.8	2.951×10^{-8}	52.2	6.457×10^{-4}	36.1	0.5			
Low-albite		9.8	2.754×10^{-13}	69.8	6.918×10^{-11}	65	0.457	2.512×10^{-16}	71	-0.572
Siderite		9.8	1.260×10^{-9}	62.76	1.590×10^{-4}	45.0	0.9			
Ankerite		9.8	1.260×10^{-9}	62.76	1.590×10^{-4}	45.0	0.9			
Dawsonite		9.8	1.260×10^{-9}	62.76	1.590×10^{-4}	45.0	0.9			
Ca-smectite		151.6	1.660×10^{-13}	35	1.047×10^{-11}	23.6	0.34	3.020×10^{-17}	58.9	-0.4
Pyrite		12.9	$k_{25}=2.818\times10^{-5}$ $E_a =56.9$ $n(O_2(aq))=0.5$		$k_{25}=3.02\times10^{-8}$ $E_a =56.9$ $n(H^+)=-0.5,\quad n(Fe^{3+})=0.5$					

We started from the initial water chemical composition (Table 3), a NaCl-dominated brine of a sample from the Frio-I test site (Kharaka et al., 2006b). A temperature of 59°C was used throughout. Aqueous complex dissociation and mineral dissolution and precipitation are modeled in terms of the primary species: H_2O, H^+, Ca^{2+}, Mg^{2+}, Na^+, K^+, Fe^{2+}, AlO_2^-, Cl^-, SO_4^{2-}, HCO_3^-, $O_2(aq)$, and $SiO_2(aq)$. A total of 38 aqueous complexes were considered, including OH^-, $CO_2(aq)$, CO_3^{2-}, $CaCO_3(aq)$, $NaCO_3^-$, $FeHCO_3^+$, $FeCO_3(aq)$, $NaHCO_3(aq)$, $CaHCO_3^+$, and $MgHCO_3^+$. Activity coefficients of aqueous species are calculated from the extended Debye-Hückel equation (Helgeson et

al., 1981) as implemented in TOUGHREACT. The calculated ionic strength for initial water is 1.6.

Table 3. Initial total dissolved component concentrations, derived from baseline fluid samples collected prior to CO_2 injection (Kharaka et al., 2006b). $O_2(aq)$ concentration was obtained by equilibrium with initial mineral composition. Iron is the sum of Fe^{2+} and Fe^{3+} and their related complexes (mainly Fe^{2+}). Carbon is the sum of $CO_2(aq)$, $CH_4(aq)$, and their related species such as HCO_3^- and acetic acid(aq). Sulfur is the sum of sulfate and sulfide species

Component	Concentration (mol/kg H_2O)
Ca^{2+}	6.6×10^{-2}
Mg^{2+}	2.2×10^{-2}
Na^+	1.35
K^+	4.53×10^{-3}
Iron	4.63×10^{-4}
$SiO_2(aq)$	2.50×10^{-4}
Carbon	5.04×10^{-2}
Sulfur	4.20×10^{-5}
Al^{3+}	1.56×10^{-8}
Cl^-	1.49
$O_2(aq)$	4.88×10^{-68}
pH	6.7
Temperature	$59^{\circ}C$

Prior to simulating reactive transport, batch geochemical modeling of water-rock interaction was performed to equilibrate the measured chemical composition with the primary minerals listed in Table 2 at a CO_2 gas pressure of 0.15 bar and a temperature of $59^{\circ}C$. The background (initial) CO_2 gas pressure was chosen to match the measured pH. A reasonably short simulation time (10 years in the present study) is needed to obtain nearly steady-state aqueous solution composition for the reactive transport simulation.

4.3. Thermodynamic data

The primary source for equilibrium constants for aqueous species and minerals used originated with the EQ3/6 V7.2b database (Wolery, 1992), previously generated

from thermodynamic data using SUPCRT92 (Johnson et al., 1992). However, the thermodynamic properties of several minerals and aqueous species have been revised along the work of Xu et al. (2005, 2007). The thermodynamic properties of dolomite and magnesite were calculated, using the Gibbs free energy values determined by Rock et al. (2001), together with the respective entropies provided by Robie and Hemingway (1995). In the presented study, the thermodynamic properties of siderite are refined based on Bénézeth et al. (2009). These, together with entropy data for end-member ankerite, $CaFe(CO_3)_2$, from Holland and Powell (1998) were used to calculate the properties of end-member ankerite and the ankerite ideal binary solid solution with the limiting composition: $CaMg_{0.3}Fe_{0.7}(CO_3)_2$, using the lattice energy calculations reported by Chai and Navrotsky (1996). In this study, the properties of dawsonite are updated according to Bénézeth et al. (2007).

Uncertainties relating to the thermodynamic properties of the ferrous and ferric ions in aqueous solution have bedeviled precise modeling of geochemical systems involving these species for some time (Reardon and Beckie, 1987). We therefore incorporated revised properties of Fe^{2+} and Fe^{3+} in SUPCRT92 and recalculated the solubility products of all participating iron-containing minerals whose thermodynamic properties were derived from calorimetry. These included chlorite, pyrite, and hematite, as well as appropriate corrections to the solubility products of siderite and ankerite. To ensure consistency with unmodified equilibrium constants in the EQ3/6 V7.2b database, all revised thermodynamic data were incorporated in the SUPCRT92 database and new equilibrium constants similarly generated.

4.4. Kinetics of mineral dissolution and precipitation

Dissolution and precipitation of all minerals proceeds under kinetic conditions. Kinetic rates are a product of the rate constant and reactive surface area (Eq. A.1 in Appendix A). Multiple mechanisms (including neutral, acid and base) are used for dissolution of minerals (Eqs. A.2 and A.3 in Appendix A). Kinetic parameters including rate constant (k_{25}), the activation energy (E_a), and the power term (n) for each mechanism are also listed in Table 2. At any pH the total rate is the sum of the rates via each mechanism. Rate law parameters for kaolinite, illite, chlorite, albite-low, oligoclase, K-

feldspar, magnesite, and dolomite were taken from Palandri and Kharaka (2004), who compiled and fitted experimental data reported by many investigators. The detailed list of the original data sources is given in Palandri and Kharaka (2004). Illite kinetic data were set to those of smectite. Siderite kinetic data for neutral mechanism were from Knauss et al (2005), and that for acid mechanism from Golubev et al. (2009). Ankerite and dawsonite kinetic data were set to these of siderite.

Mineral reactive-surface areas (the third column of Table 2) are based on the work of Sonnenthal et al. (2005), and were calculated assuming a cubic array of truncated spheres constituting the rock framework. The larger surface areas for clay minerals (kaolinite, illite, smectite and chlorite) are due to smaller grain sizes. In conformity with White and Peterson (1990) and Zerai et al. (2006), a surface roughness factor of 10 is incorporated and defined as the ratio of the true (BET) surface area to the equivalent geometric surface area. Interaction with the minerals is generally expected to occur only at selective sites of the mineral surface, and the actual reactive surface area could be between one and three orders of magnitude less than the surface roughness-based surface area (Lasaga, 1995; Zerai et al. 2006). The difference is attributed to the fact that only part of the mineral surface is involved in the reaction due to coating or armoring, a small area exposed to the brine, and channeling of the reactive fluid flow. To account for these effects, the actual reactive surface areas given in Table 2 are decreased by two orders of magnitude from the surface roughness-based surface areas. The reactive surface areas used here for most minerals are similar to those of Zerai et al. (2006) and Knauss et al. (2005), who used a surface area of about 10 cm^2/g mineral.

If the aqueous phase supersaturates with respect to a potential secondary mineral, a small volume faction such as 1×10^{-6} is used for calculating the seed surface area for the new phase to grow. The precipitation of secondary minerals is represented using the same kinetic expression as that for dissolution. However, because precipitation rate data for most minerals are unavailable, parameters for neutral pH rates only, as given in Table 2, were employed to describe precipitation. Multiple kinetic mechanisms for precipitation can be specified in an input file of the TOUGHREACT program, should such information become available.

The evolution of the surface area in natural geologic media is very complex, especially for multi-mineral systems, and is not quantitatively understood at present. The magnitudes of surface areas specified are highly uncertain. Xu et al. (2005) performed sensitivity simulations regarding ankerite and dawsonite precipitation kinetics, and results indicated that changes in the reaction rate result in small changes in their precipitation because the precipitation requires reactants whose availability is controlled by the slow dissolution of aluminosilicate minerals.

4.5. A kinetic model for Fe release to the aqueous phase

The large increases observed in concentrations of dissolved Fe (mainly Fe^{2+}) and bicarbonate could result from dissolution of siderite, but no siderite was observed in the retrieved core (Kharaka et al., 2006b). Hence, these increases are likely caused by dissolution of iron oxyhydroxides. Alternatively, the release of Fe into the aqueous phase could be caused by desorption of Fe from mineral surface (Kharaka et al., 2009). Recent SEM with EDAX analyses by McGuire and Grigsby (2009) identified that clay grain coats contain Fe, Si, O, Al, K, and Na. There was discussion on that some of increases in dissolved Fe could be from the corrosion of pipe and well casing that contact with the low pH brine (Kharaka et al., 2009). Recent laboratory experiments conducted by Carroll (2009) in metal-free equipment, indicate that the Fe release is from reaction of the acid brine with the sediment. The experiment has not determined the Fe are desorbed from a mineral substrate or dissolved from its incorporation in mineral phases.

In this work, we assume that the Fe is released from the sediment. We intend to model the distribution of Fe between the aqueous and solid phases. The solid can be Fe-bearing mineral phases or Fe sorption sites, and we simply denote it as Fe(ads). It is commonly understood that the Fe release (by dissolution and/or desorption) is due to lowering of pH as a result of CO_2 injection. In this work, a kinetic Fe release model was developed by assuming the following release reaction, two orders in terms of H^+:

$$Fe(ads) + 2H^+ \rightarrow Fe^{2+}(aq) \tag{1}$$
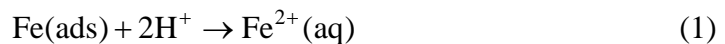
If reaction (1) follows a simple path (no intermediate steps), its net rate r can be given by the difference between the forwards and backwards rates, or:

$$r = k_f \left(Fe(ads) \right) \left(H^+ \right)^2 - k_b \left(Fe^{2+}(aq) \right)$$ (2)

where ( ) represents the activity of a species. The forward rate is assumed to be proportional to forward rate constant k_f multiplying reactant Fe(ads) activity and reactant H^+ activity with a power term of two (reaction order). The backward rate is assumed to be proportional to backward rate constant k_b multiplying $Fe^{2+}(aq)$ activity. Initially the system is assumed to be at chemical equilibrium, the forward rate is equal to the backward rate or r = 0. Therefore, we have:

$$k_b = \frac{\left(Fe(ads) \right) \left(H^+ \right)^2}{\left(Fe^{2+}(aq) \right)} k_f$$ (3)

From the field measurements, we know that initially the $Fe^{2+}(aq)$ concentration is 3.852×10^{-4} mol/kg H_2O, and H^+ activity is 2.571×10^{-7}. $Fe^{2+}(aq)$ activity coefficient is 0.143, according to the speciation of the initial water composition (Table 3). Calculation methods for aqueous activity coefficients and ionic strength have been already discussed in Section 4.2 'Geochemical System'. We do not know activity Fe(ads) and parameter k_f a priori, so we tried different set of values in r (Eq. 2) until the model could reproduce the Fe concentration breakthrough curve (Figure 6b). Assuming a Fe(ads) activity coefficient of one, a Fe(ads) concentration of 3×10^{-2} mol/kg H_2O, and a k_f value of 2.2224×10^4 matches well with observations.

An increase in dissolved Mn concentration was observed too at the Frio-I Pilot test performed in October 2004, but Zn and Pb concentrations were not measured at this field experiment. Increases in dissolved Zn and Pb were observed in laboratory experiments (Carroll, 2009) and other field experiments (Kharaka et al., 2009). A similar form of their release rates (but with different parameters) may be written. However, compared to Fe, the Mn, Zn, and Pb related mineral phases, adsorption sites,

thermodynamic and kinetic data are not well understood. Additional investigations are required to study the behavior of these heavy metals in the future.

5. Results and Discussion

5.1. Changes in water chemistry

After being injected, supercritical CO_2 (called "gas" here) moves away from the injection well (Figure 3a). The simulations show that after about 3 days, CO_2 gas breakthrough occurs at the observation well 30 m away (Figure 3b). Note that injection was stopped at about 10 days. CO_2 gas dissolution into brine lowers the pH, and the pH front advances with the gas phase (Figure 4a). After the breakthrough, the modeled pH drops to 3.5 at the observation well (Figure 3b). This pH value is reasonably close to ~3, the initial pH value computed by Kharaka et al. (2009) prior to mineral dissolution and at subsurface temperature of 60ºC and pCO_2 of 150 bar. The pH values measured at surface after breakthrough, but CO_2 degassing were ≥ 5.7 (Kharaka et al., 2006b). The modeled pH gradually increases to 4.7 due to calcite dissolution. Differences between simulated and observed pH are attributed to degassing from samples that occurred prior to the surface measurement. Other possible causes for the difference are including waters from layers with and without CO_2 in the sample, and discrepancies associated with difference in mineralogy and fluid composition among layers. The measured pH is a mean value. After breakthrough, simulated HCO_3^- concentrations increase because CO_2 gas dissolution into brine. The modeled HCO_3^- concentration increases capture the observed values reasonably well (Figure 5b).
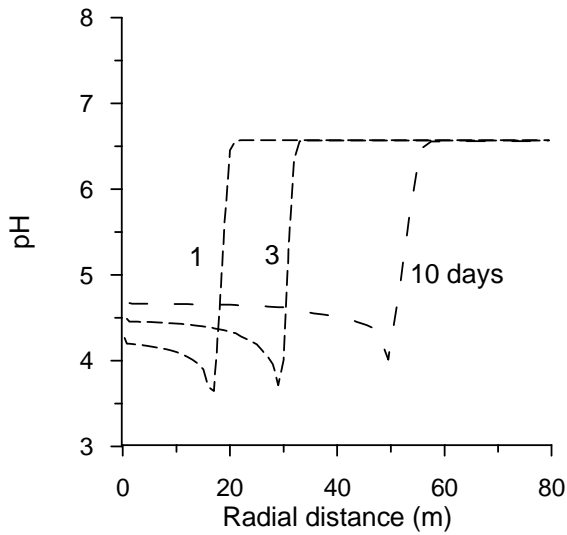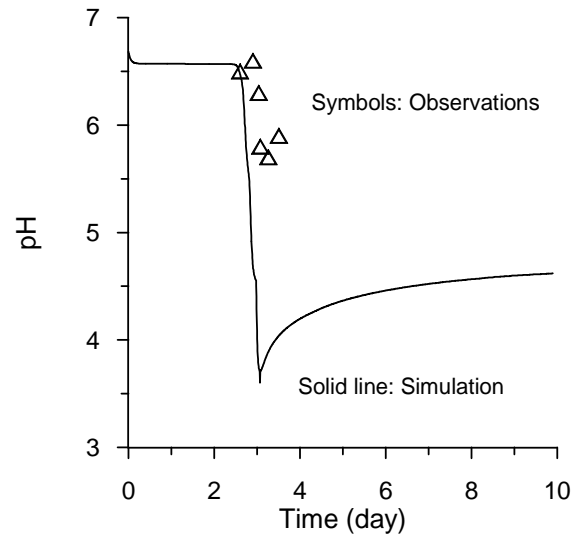
16
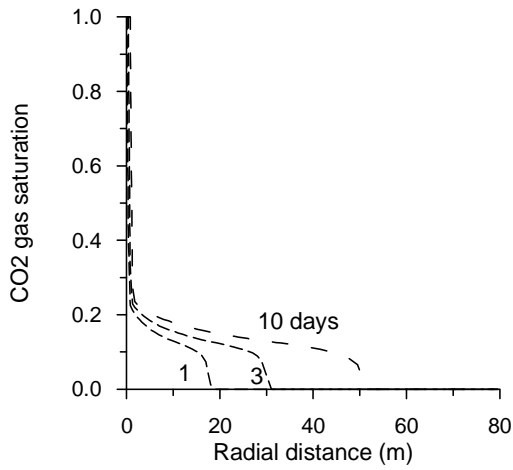
(a) Spatial distribution
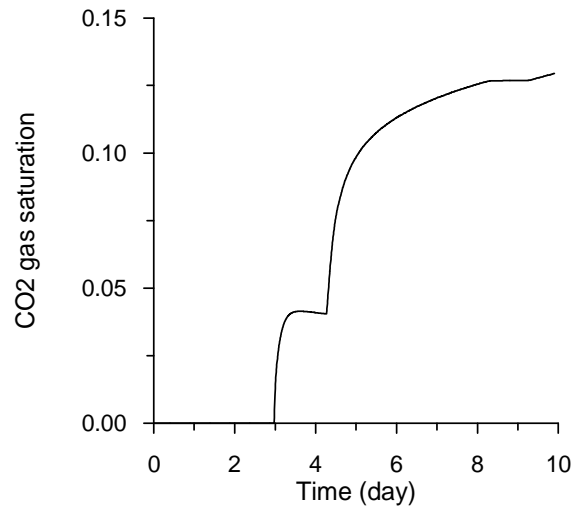
(b) Time evolution

Figure 3. Simulated supercritical CO_2 (gas) saturation. (a) Spatial distribution at different times, and (b) Time evolution at the observation well (30 m from the injection well).

(b) Time evolution

(a) Spatial distribution

Figure 4. Simulated pH profile. (a) Spatial distribution at different times, and (b) Time evolution at the observation well.
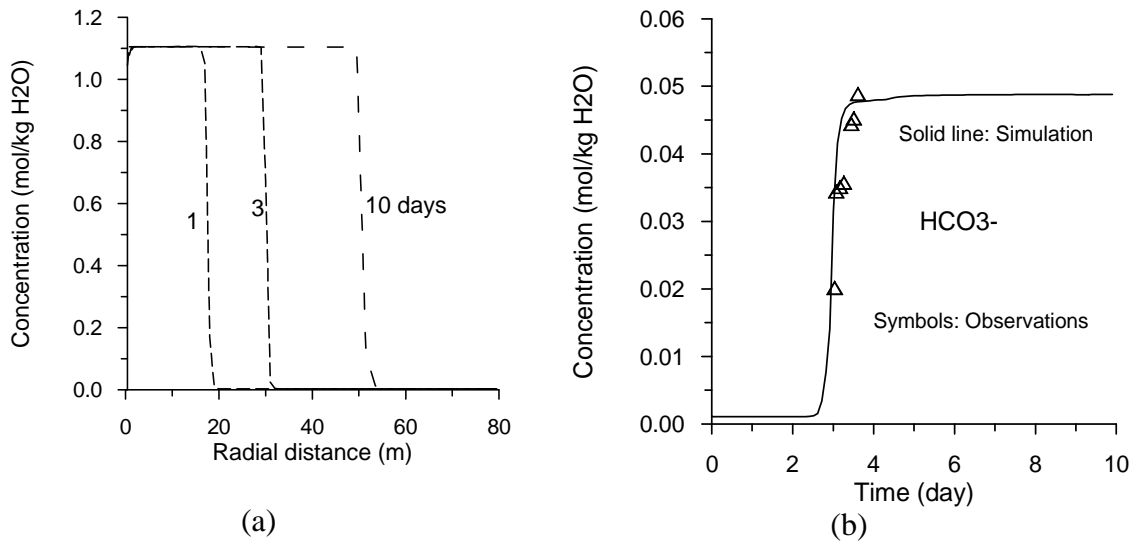
17

Figure 5. (a) Spatial distribution of total dissolved CO_2 at different times, and (b) Time evolution of HCO_3^- species concentration at the observation well.

The lowered pH induces Fe release to the aqueous phase either from dissolution of Fe solid phases and/or desorption from mineral surfaces, which increases aqueous Fe concentration (Figure 6b). The kinetic release model with a calibrated initial Fe(ads) concentration (3×10^{-2} mol/kg H_2O as mentioned in Section 4.5) can reproduce the increases in Fe^{2+}(aq) concentration that were observed following the CO_2 breakthrough (Figure 6b). After 0.2 years (73 days), carbonate minerals siderite and ankerite start to precipitate (Figure 7). Consequently, dissolved Fe concentrations decrease (Figure 8). The simulated trend is consistent with observation. In the observation, dissolved Fe decreases to 0.0046 mol/kg (250 ppm) after 0.5 years. While, the base-case simulation predicts that the observed value of Fe occurred at about 0.65 years not 0.5 years. To obtain a better match, we performed an additional simulation with siderite and ankerite rate constants in Table 2 increased by a factor 1.25. The additional simulation captures well the observed value of Fe occurred at about 0.5 years (Figure 8).

18
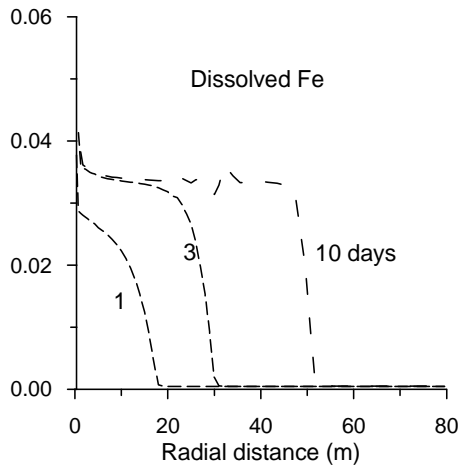
(a) Spatial distribution
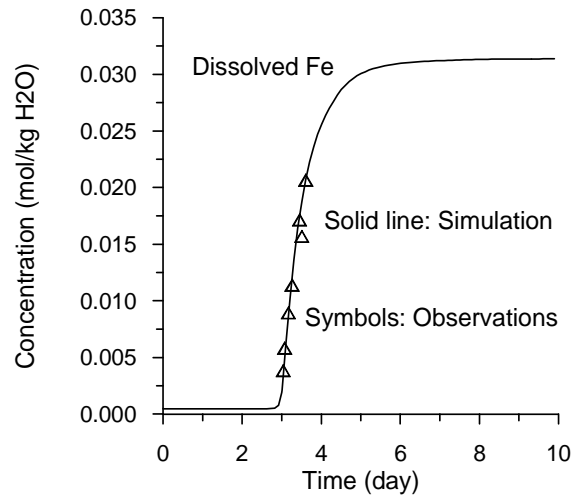
(b) Time evolution

Figure 6. Profile of dissolved Fe (mainly Fe^{2+}(aq)) concentration. (a) Spatial distribution at different times, and (b) Time evolution at the observation well.
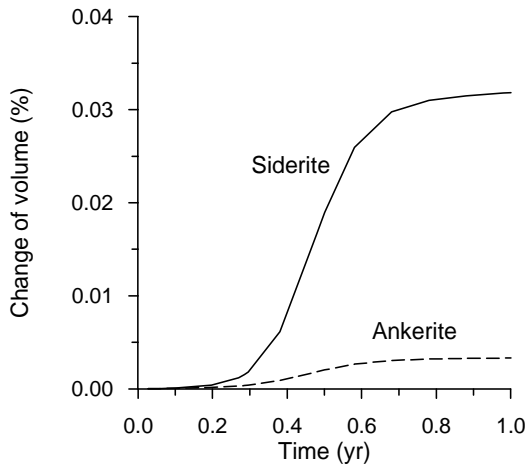

Figure 7. Simulated precipitation (in volume fraction) of siderite and ankerite at the observation well for a period of one year.
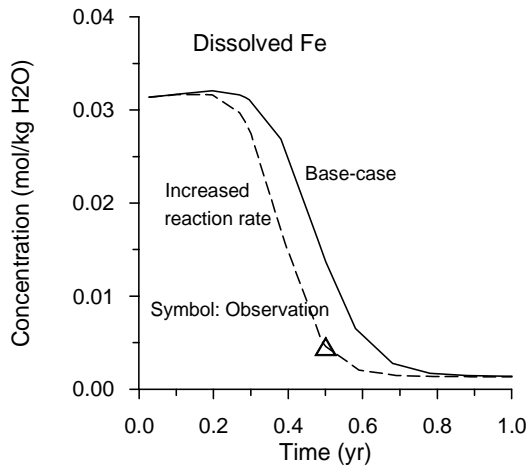
Figure 8. Evolution of dissolved Fe concentration at the observation well for a period of one year.

5.2. Long-term CO_2 sequestration

A simulation of 1,000 years was performed to understand the long-term evolution of injected CO_2 among gas, liquid and solid phases. The simulation was not meant to duplicate the local Frio Sandstone structure, which is steeply dipping due to the close proximity to a salt dome, but is rather suggestive of the long-term behavior of a plume which is essentially stratigraphically trapped beneath a confining layer. Figure 9a shows CO_2 gas saturations along the radial distance (water saturations are complementary to gas saturations, or $S_l = 1 - S_g$). The CO_2 plume (two-phase region) gradually spreads outward due to capillary forces, and the gas saturation gradually decreases as supercritical CO_2 dissolves to replace aqueous CO_2 consumed by formation of secondary carbonate minerals (see Figure 10). After 500 years, the CO_2 gas phase disappears completely. The dissolved (aqueous) CO_2 remains, but gradually decreases due to carbonate precipitation (Figure 9b).
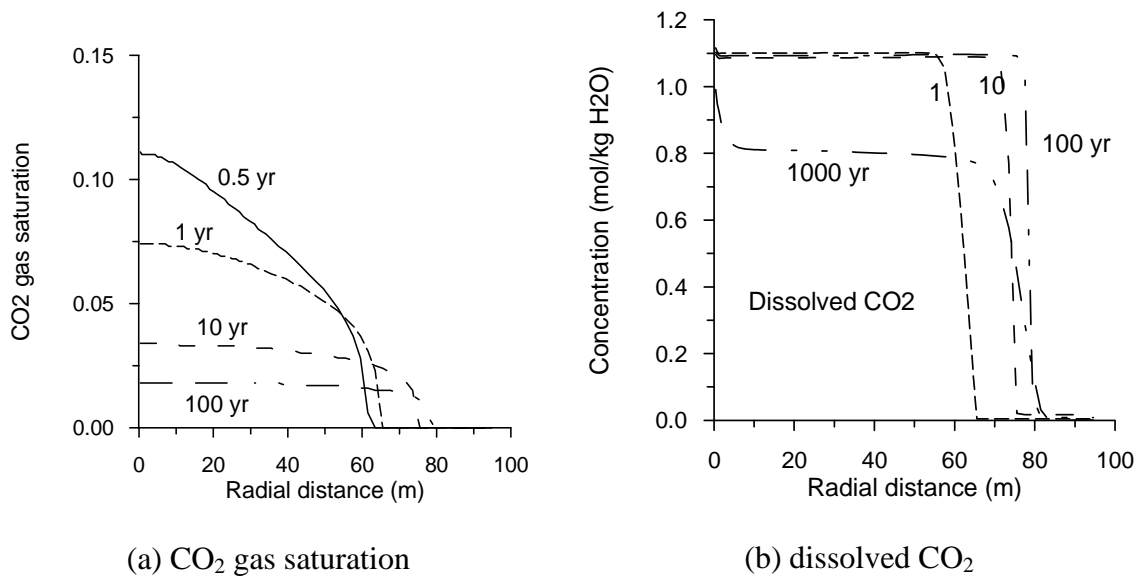
| (a) CO_2 gas saturation | (b) dissolved CO_2 |

Figure 9. Distribution of CO_2 gas saturation (a) and dissolved CO_2 concentrations (b) at different times for the long-term simulation.

Changes in volume fraction of carbonate minerals at different times are presented in Figure 10. Although calcite was initially present in the formation, it is completely dissolved after 150 years in the CO_2 plume region (Figure 10a). In the background region (beyond 75 m), a small amount of calcite dissolution occurs. Siderite initially precipitates until 100 years but later dissolves completely (Figure 10b). Ankerite appears after 100 years, and is a stable carbonate phase (Figure 10c). Close to 1% volume fraction of ankerite is formed after 1,000 years. Note that dissolution of one mole of calcite ($CaCO_3$) and 0.7 mole of siderite ($FeCO_3$) leads to the precipitation of one mole of ankerite $CaMg_{0.3}Fe_{0.7}(CO_3)_2$, with extra moles of (Mg) and (CO_3) entities. Therefore, the net balance for the formation of ankerite is CO_2 mineral trapping. A small amount of dawsonite forms after 100 years. Some kaolinite precipitates in the CO_2 plume region (Figure 11a). Significant precipitation of illite was obtained (Figure 11b).
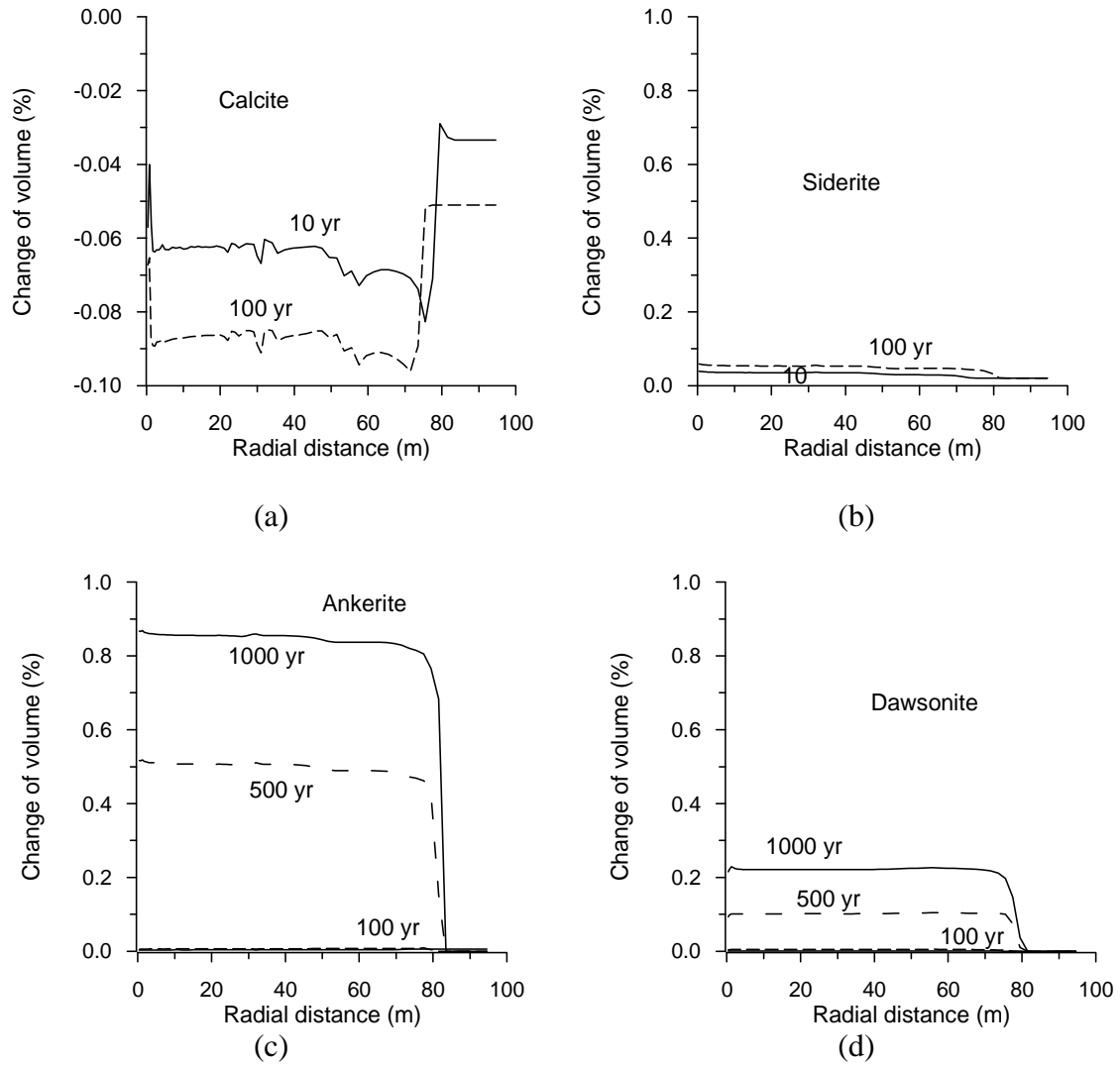
Figure 10. Dissolution and precipitation of carbonate minerals (in change of volume fraction, negative values indicate dissolution and positive precipitation) for the long-term simulation.
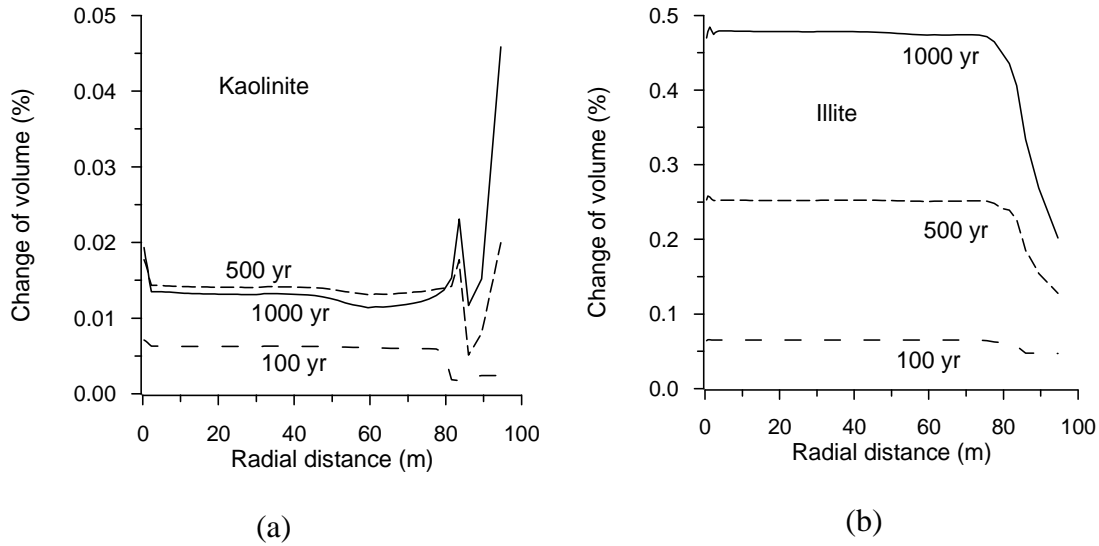
Figure 11. Precipitation of clay minerals (in percentage of volume fraction) for the long-term simulation.

The cumulative sequestration of CO_2 by secondary carbonates is presented in Figure 12. The curve at 10 years shows a negative mineral trapping, indicating calcite dissolution dominate initially. Significant CO_2 mineral trapping starts at 100 years and increases with time, because of ankerite and dawsonite precipitation. After 1,000 years, the CO_2 mineral trapping can reach about 9 kg/m^3 medium. The trapping capability depends on the primary mineral composition. Precipitation of siderite and ankerite requires Fe^{2+} supplied by the dissolution of iron-bearing minerals, such as chlorite, and by reduction of Fe^{3+} in small amounts of hematite. As mentioned above, oligoclase was assumed to have a 1:4 of anorthite ($CaAl_2Si_2O_8$) over albite ($NaAlSi_3O_8$). Variation in Ca content in oligoclase affects carbonate mineral precipitation, and thus amounts of CO_2 mineral trapping (Zhang et al., 2009).

The time required for mineral alteration and CO_2 sequestration depends on the rates of mineral dissolution and precipitation, which are products of the kinetic rate constant and reactive surface area. Scaling kinetic rates for all minerals by the same factor is equivalent to scaling the time coordinate (Xu et al., 2005). Such changes result in reciprocal changes to the time scale. Zhang et al. (2009) performed sensitivity

23

simulations regarding abundance of chlorite and oligoclase, indicating that changes in their abundance affect the estimates of mineral alteration and CO_2 storage capacity.
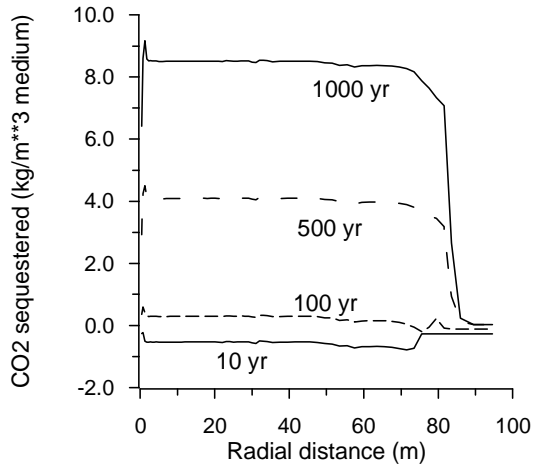

Figure 12. CO_2 sequestered by carbonate minerals at different times for the long-term simulation.

The current simulated mineral alteration pattern is generally consistent with available mineralogy observed at natural high-pressure CO_2 gas reservoirs. An example is that by Moore et al. (2005), who describe the formation of secondary dawsonite and kaolinite in siltstones of the Permian Supai Formation of the Springerville-St. John CO_2 field on the border between Arizona and New Mexico, USA. They observed secondary dawsonite spatially associated with corroded oligoclase and K-feldspar, which is consistent with our simulations. Furthermore, their determination that kaolinite formed subsequent to dawsonite deposition following a decline in the CO_2 pressure, is also consistent with our finding that kaolinite is unstable during the precipitation of dawsonite. Illite appears to persist in the presence of dawsonite, which is also consistent with our modeling results. In contrast, the Supai Formation appears to have been more oxidizing, with a limited capacity to provide Fe^{2+} for the stabilization of ankerite.

Another paper (Watson et al., 2004) describes mineralogical and groundwater changes caused by magmatic carbon dioxide invading a gas reservoir in a lithic sandstone of the Pretty Hill Formation in the Ladbroke Grove gas field in South Australia. An important feature of this field example is that the mineralogy can be compared with an

24

adjacent unmodified methane gas reservoir in the same formation. In contrast to those of the Supai Formation of Arizona and New Mexico, the conditions in this high-pressure CO_2 field are such that Fe^{2+} is available for the stabilization of siderite and ankerite. In this respect, the Ladbroke Grove field more closely represents the conditions of our simulation. Observed similarities include the destruction of chlorite in the lithic fragments and net corrosion of the feldspars, a reduction in the concentration of calcite, an increase in the concentration of siderite, a significant increase in the quantity of ankerite. However, no dawsonite was reported even though an evaluation of the coexisting groundwater indicates that it should have been supersaturated with respect to this carbonate. A substantial increase in the concentration of kaolinite is observed, which is in conflict with our simulation. The differences might be explained by the higher Cl^- and Na^+ concentrations in the present simulation.

Recently, Gao et al. (2009) reported that a CO_2 gas reservoir sandstones in the Hailaer Basin (Northeastern China) contain abundant dawsonite as a cement and replacement mineral. The origins of dawsonite and CO_2 in these sandstones were studied by petrographic and isotopic analysis. According to the paragenetic sequence of the sandstones, dawsonite grew later than CO_2 charging at 110-85 Ma. Besides dawsonite, the cements in dawsonite-bearing sandstones include quartz overgrowths, ankerite and clay minerals, which are consistent with our simulation results.

6. Summary and Conclusions

Based on a calibrated 1-D radial flow model, reactive transport modeling was performed for the Frio-I Brine Pilot, a small-scale CO_2 sequestration test. Increases in HCO_3^- concentration were well reproduced by an initial simulation. A very simple kinetic model of iron (Fe) release from the solid to aqueous phase was developed, which can reproduce the increases in aqueous Fe concentration following the CO_2 breakthrough. After half a year, observed aqueous Fe concentrations decrease due to carbonate precipitation, this trend can be also captured by our modeling. The model developed here can estimate potential mobile Fe inventory, and its bounding concentration in the storage formation from limited observation data. The method may be useful for future studies on mobility of other heavy metals such as Zn and Pb.

Simulations of long-term behavior show that the CO_2 plume gradually spreads outward due to capillary forces, and the gas saturation gradually decreases due to dissolution and the formation of carbonates. The CO_2 gas phase is predicted to disappear after 500 years. Elevated aqueous CO_2 concentrations remain for a longer time, but eventually decrease due to precipitation of carbonates. For the Frio-I Brine Pilot, all injected CO_2 could ultimately be sequestered as carbonate minerals. The information currently available for the mineralogy of natural high-pressure CO_2 gas reservoirs is generally consistent with our simulation.

Further laboratory experiments are needed to obtain detailed Fe and Mn mineralogical composition on the surface coating of mineral grains and to find out the mechanism of the metal release, dissolution, or/and desorption. Additional laboratory, field, and modeling investigations are proposed to better understand changes in dissolved organic carbon and isotope composition.

References

Allen, D.E., Strazisar, B.R., Soong, Y., Hedges, S.W., 2005. Modeling carbon dioxide sequestration in saline aquifers: Significance of elevated pressures and salinities. Fuel Process. Technol. 86, 1569-1580.

Bachu, S., Gunter, W.D., Perkins, E.H., 1994. Aquifer disposal of CO_2: hydrodynamic and mineral trapping. Energy Convers. Mgmt. 35, 269-279.

Bénézeth, P.,Palmer, A.D., Anovitz, L.M., Horita, J., 2007. Dawsonite synthesis and reevaluation of its thermodynamic properties from solubility measurements: Implications for mineral trapping of CO_2. Geochimica et Cosmochimica Acta 71, 4438-4455.

Bénézeth, P., Dandurand, J.L., Harrichoury, J.C., 2009. Solubility product of siderite ($FeCO_3$) as a function of temperature (25–250 °C). Chem. Geol., 265 3-12.

Carroll, S., 2009. Trace metal release from Frio sandstone reacted with CO_2 and 1.5 NaCl Brine at 60^oC. In proceedings: Eighth Annual Conference on Carbon Capture & Sequestration, Pittsburgh, Pennsylvania.

Chen, Z., O'Connor, W.K., Gerdemann, S.J., 2006. Carbonation for carbon sequestration and explanation of experimental results. Environ. Prog. 25, 161-166.

Corey, A. T., 1954. The interrelation between gas and oil relative permeabilities, Producers Monthly 19(1), 38-41.

Chai, L., Navrotsky, A., 1996. Synthesis, characterization, and energetics of solid solution along the dolomite-ankerite join, and implications for the stability of ordered CaFe(CO3)2. American Mineralogist 81, 1141-1147.

Doughty, C. and Pruess, K., 2004. Modeling supercritical carbon dioxide injection in heterogeneous porous media. Vadose Zone Journal 3(3), 837-847.

Doughty, C., Freifeld, B.M., and Trautz, R.C., 2008. Site characterization for CO_2 geologic storage and vice versa – the Frio brine pilot, Texas, USA as a case study. Environmental Geology 54(8), 1635-1656.

Freifeld, B.M., Trautz, R.C., Kharaka, Y.K., Phelps, T.J., Myer, L.R., Hovorka, S.D., and Collins, D.J., 2005. The U-tube: A novel system for acquiring borehole fluid samples from a deep geologic CO_2 sequestration experiment: J. Geophys. Res. 110, B10203.

Gao, Y., Liu, L., Hua, W., 2009. Petrology and isotopic geochemistry of dawsonite-bearing sandstones in Hailaer basin, northeastern China. Appl. Geochem. 24, 1724-1738.

Gaus, I., Azaroual, M., Czernichowski-Lauriol, I., 2005. Reactive transport modeling of the impact of CO_2 injection on the clayey cap rock at Sleipner (North Sea). Chem. Geol. 217, 319-337.

Golubev, S.V., Bénézeth, P., Schott, J., Dandurand, J.L., Castillo, A., 2009. Siderite dissolution kinetics in acidic aqueous solutions from 25 to 100°C and 0 to 50 atm pCO_2. Chem. Geol. 265, 13-19.

Gunter, W.D., Perkins, E.H., Hutcheon, I., 2000. Aquifer disposal of acid gases: modeling of water-rock reactions for trapping of acid wastes. Appl. Geochem. 15, 1085-1095.

Helgeson, H.C., Kirkham, D.H., Flowers, G.C., 1981. Theoretical prediction of the thermodynamic behavior of aqueous electrolytes at high pressures and temperatures: IV. Calculation of activity coefficients, osmotic coefficients, and apparent molal and standard and relative partial molal properties to 600 C and 5 kb. Am. J. Sci. 281, 1249–1516.

Hitchon, B., Gunter, W.D., Gentzis, T., Bailey, R.T., 1999. Sedimentary basins and greenhouse gases: a serendipitous association. Energy Convers. Manage. 40, 825-843.

Holland, T.J.B., Powell, R., 1998. In internally consistent thermodynamic data set for phases of petrological interest. Journal of Metamorphic Geology 16(3), 309-343.

Hovorka, S.D., Benson, S.M., Doughty, C.K., Freifeld, B.M., Sakurai, S., Daley, T.M., Kharaka, Y.K., Holtz, M.H., Trautz, R.C., Nance, H.S., Myer, L.R., and Knauss, K.G., 2006. Measuring permanence of CO_2 storage in saline formations-The Frio experiment. Environmental Geosciences 13, 103–119.

Johnson, J.W., Oelkers, E.H., Helgeson, H.C., 1992. SUPCRT92: A software package for calculating the standard molal thermodynamic properties of minerals, gases, aqueous species, and reactions from 1 to 5000 bars and 0 to 1000 degrees C. Computers and Geosciences 18, 899–947.

Knauss, K.G., Johnson, J.W., Steefel, C.I., 2005. Evaluation of the impact of CO_2, co-contaminant gas, aqueous fluid, and reservoir rock interactions on the geologic sequestration of CO_2. Chem. Geol. 217, 339-350.

Kharaka, Y.K., Cole, D.R., Thordsen, J.J., Kakouros, E., Nance, H.S., 2006a. Gas–water–rock interactions in sedimentary basins: CO_2 sequestration in the Frio Formation, Texas, USA. Journal of Geochemical Exploration 89, 183–186.

Kharaka, Y.K., Cole, D.R., Hovorka, S.D., Gunter, W.D., Knauss, K.G., Freifeld, B.M., 2006b. Gas-water-rock interactions in Frio Formation following CO2 injection:

Implications for the storage of greenhouse gases in sedimentary basins. Geology, 34(7), 577-580.

Kharaka, Y.K., and Hanor, J.S., 2007, Deep fluid in the continents: I. Sedimentary basins. *in* Treatise on geochemistry, Volume 5, Surface and ground water, weathering, and soils: Oxford, UK, Elsevier-Pergamon, p. 1-48.

Kharaka, Y. K., Thordsen, T. T., Hovorka, S. D., Nance, S., Cole, D. R., Phelps, T. J., Knauss, K. G., 2009. Potential environmental issues of CO_2 storage in deep saline aquifers: Geochemical results from the Frio-I Brine Pilot test, Texas, USA. Appl. Geochem. 24, 1106-1112.

Lasaga, A.C., Soler, J.M., Ganor, J., Burch, T.E., Nagy, K.L., 1994. Chemical weathering rate laws and global geochemical cycles. Geochimica et Cosmochimica Acta 58, 2361-2386.

Lasaga, A.C., 1995. Fundamental approaches in describing mineral dissolution and precipitation rates. In: White, A.F., Brantley, S.L. (Eds.), Chemical Weathering Rates of Silicates Minerals, Reviews in Mineralogy, vol. 31. BookCrafters, Chelsea, MI, pp. 23–86.

McGuire, K., Grigsby, J.D., 2009. Petrographic and geochemical characterization of the Frio Formation, Texas: Implications of CO_2 Sequestration. AAPG Annual Convention and Exhibition, Denver, Colorado, (June 7-10, 2009).

Moore, J., Adams, M., Allis, R., Lutz, S., Rauzi, S., 2005. Mineralogical and geochemical consequences of the long-term presence of CO_2 in natural reservoirs: An example from the Springerville–St. Johns Field, Arizona, and New Mexico, U.S.A. Chem. Geol. 217, 365-385.

Newton, R.C., Charlu, T.V., Kleppa, O.J., 1980. Thermochemistry of the high structural state plagioclases. Geochim. Cosmochim. Acta 44, 933-942

Palandri, J., Kharaka, Y.K., 2004. A compilation of rate parameters of water-mineral interaction kinetics for application to geochemical modeling. US Geol. Surv. Open File Report 2004-1068, 64 pp.

Parkhurst, D.L., Appelo, C.A.J., 1999. User's Guide to PHREEQC (Version 2) - A computer program for speciation, batch-reaction, one-dimensional transport, and

inverse geochemical calculations. USGS Water-Resources Investigations Report 99-4259, Denver, Colorado.

Pokrovsky, O. S., Golubev, S.V., Jordan, G., 2009. Effect of organic and inorganic ligands on calcite and magnesite dissolution rates at 60 °C and 30 atm pCO_2, Chem. Geol., 265, 33-43.

Pruess, K., 2004. The TOUGH Codes - A family of simulation tools for multiphase flow and transport processes in permeable media. Vadose Zone Journal 3, 738-746.

Reardon, E.J., Beckie, R.D., 1987. Modelling chemical equilibria of acid mine drainage: The FeSO4-H2SO4-H2O system. Geochim. et Cosmochim. Acta 51, 2355-2368.

Robie, R.A., Hemingway, B.S., 1995. Thermodynamic properties of minerals and related substances at 298.15 K and 1 bar (10^5 Pascals) pressure and at higher temperatures. U.S. Geol. Surv. Bull. 2131, 461 p.

Rock, P.A., Mandell, G.K., Casey, W.H., Walling, E.M., 2001. Gibbs energy of formation of dolomite from electrochemical cell measurements and theoretical calculations. Am. J. Sci. 301, 103-111.

Soong, Y., Goodman, A.L., McCarthy-Jones, J.R., Baltrus, J.P., 2004. Experimental and simulation studies on mineral trapping of CO_2 with brine. Energy Convers. Manage. 45, 1845-1859.

Spycher, N., Pruess, K.,2005. CO_2-H_2O mixtures in the geological sequestration of CO_2: II. Partitioning in chloride brines at 12–100°C and up to 600 bar. Geochimica et Cosmochimica Acta 69, 3309-3320.

Steefel, C.I., Lasaga, A.C., 1994. A coupled model for transport of multiple chemical species and kinetic precipitation/dissolution reactions with applications to reactive flow in single phase hydrothermal system. Am. J. Sci. 294, 529-592.

Sonnenthal, E., Ito, A., Spycher, N., Yui, M., Apps, J., Sugita, Y., Conrad, M., Kawakami, S., 2005. Approaches to modeling coupled thermal, hydrological, and chemical processes in the Drift Scale Heater Test at Yucca Mountain. Int. J. Rock Mech. Min. Sci. 42, 6987-719.

Van Genuchten, M. Th., 1980. A Closed-form equation for predicting the hydraulic conductivity of unsaturated soils. Soil Sci. Soc. Am. J. 44, 892 – 898.

Watson, M.N., Zwingmann, N., Lemon, N.M., 2004. The Ladbroke Grove–Katnook

carbon dioxide natural laboratory: A recent CO_2 accumulation in a lithic sandstone reservoir. Energy, 29(9-10), 1457-1466.

White, A.F., Peterson, M.L., 1990. Role of reactive surface area characterization in geochemical models. Chemical modeling of aqueous systems II. In: Melchior, D.C., Bassett, R.L. (Eds.). Am. Chem. Soc. Symp. Ser. 416, 416-475.

White, S.P., Allis, R.G., Moore, J., Chidsey, T., Morgan, C., Cwynn, W., Adams, M., 2005. Simulation of reactive transport of injected CO_2 on the Colorado Plateau, Utah, USA. Chem. Geol. 217, 387-405.

Wolery, T.J., 1992. EQ3/6: Software package for geochemical modeling of aqueous systems: Package overview and installation guide (version 7.0). Lawrence Livermore National Laboratory Report UCRL-MA-110662 PT I, Livermore, California.

Wolf, G.H., Chizmeshya, A.V.G., Diefenbacher, J., Mckelvy, M.J., 2004. In situ observation of CO_2 sequestration reactions using a novel microreaction system. Environ. Sci. Technol. 38, 932-936.

Worden, R.H., 2006. Dawsonite cement in the Triassic Lam Formation, Shabwa Basin, Yemen: A natural analogue for a potential mineral product of subsurface CO_2 storage for greenhouse gas reduction. Mar. Petrol Geol. 23, 61-77.

Xu, T., Pruess, K., 2001. Modeling multiphase non-isothermal fluid flow and reactive geochemical transport in variably saturated fractured rocks: 1. Methodology. Am. J. Sci., 301, 16-33.

Xu, T, Apps, J.A., Pruess, K., 2004. Numerical simulation to study mineral trapping for CO_2 disposal in deep aquifers, Appl. Geochem.19, 917-936.

Xu, T, Apps, J.A., Pruess, K., 2005. Mineral sequestration of carbon dioxide in a sandstone-shale system. Chem. Geol. 217, 295-318.

Xu, T., E.L. Sonnenthal, N. Spycher, and K. Pruess, 2006. TOURGHREACT: A simulation program for non-isothermal multiphase reactive geochemical transport in variably saturated geologic media. Computer & Geosciences 32, 145-165.

Xu, T., Apps, J.A., Pruess, K., Yamamoto, H., 2007. Numerical modeling of injection and mineral trapping of CO_2 with H_2S and SO_2 in a sandstone formation. Chem. Geol. 242, 319-346.

Zhang, W., Li, Y., Xu, T., Cheng, H., Zheng, Y., Xiong, P., 2009. Long-term variations of CO_2 trapped in different mechanisms in deep saline formations: A case study of the Songliao Basin, China. Greenhouse Gas Control Technologies, v3(2), 161-180.

Zerai, B., Saylor, B.Z., Matisoff, G., 2006. Computer simulation of CO_2 trapped through mineral precipitation in the Rose Run Sandstone, Ohio. Appl. Geochem. 21, 223-240.

Appendix A. Kinetic rate law for mineral dissolution and precipitation

The general rate expression used in TOUGHREACT is taken from Lasaga et al. (1994) and Steefel and Lasaga (1994):

$$r_n = \pm k_n A_n \left| 1 - \left(\frac{Q_n}{K_n} \right)^\theta \right|^\eta \tag{A.1}$$

where n denotes kinetic mineral index, positive values of r_n indicate dissolution and negative values precipitation, k_n is the rate constant (moles per unit mineral surface area and unit time) which is temperature dependent, A_n is the specific reactive surface area, K_n is the equilibrium constant for the mineral-water reaction written for the destruction of one mole of mineral n, and Q_n is the reaction quotient. The parameters θ and η must be determined from experiments; usually, but not always, they are taken equal to one.

For many minerals, the kinetic rate constant k can be summed from three different mechanisms (Lasaga et al., 1994; Palandri and Kharaka, 2004):

$$k = k_{25}^{nu} \exp\left[\frac{-E_a^{nu}}{R} \left(\frac{1}{T} - \frac{1}{298.15} \right) \right] + k_{25}^{H} \exp\left[\frac{-E_a^{H}}{R} \left(\frac{1}{T} - \frac{1}{298.15} \right) \right] a_H^{n_H}$$
$$+ k_{25}^{OH} \exp\left[\frac{-E_a^{OH}}{R} \left(\frac{1}{T} - \frac{1}{298.15} \right) \right] a_{OH}^{n_{OH}} \tag{A.2}$$

where superscripts or subscripts nu, H, and OH indicate neutral, acid and base mechanisms, respectively, E_a is the activation energy, k_{25} is the rate constant at 25°C, R is gas constant (8.314 J mol^{-1} K^{-1}), T is absolute temperature (K), a is the activity of the species; and n is power term (constant). Notice that parameters θ and η (see Eq. A.1) are assumed the same for each mechanism. The rate constant k can also depend on other species such as Al^{3+} and Fe^{3+}, or the aqueous carbonate species or the effects of organic

and inorganic ligands (Pokrovsky et al., 2009). Two or more species may be involved in one mechanism. A general form of species-dependent rate constant (extension of Eq. A.2) is coded in TOUGHREACT as

$$k = k_{25}^{nu} \exp\left[\frac{-E_a^{nu}}{R}\left(\frac{1}{T} - \frac{1}{298.15}\right)\right] + \sum_i k_{25}^i \exp\left[\frac{-E_a^i}{R}\left(\frac{1}{T} - \frac{1}{298.15}\right)\right] \prod_j a_{ij}^{n_{ij}} \quad (A.3)$$

where superscript or subscript i is the additional mechanism index, and j is the species index involved in one mechanism, which can be the primary or secondary species. TOUGHREACT currently considers up to five additional mechanisms and up to five species involved in each mechanism.